Current-induced switching of thin film α-Fe_2O_3 devices imaged using a scanning single-spin microscope

Qiaochu Guo,[1] Anthony D'Addario,[2] Yang Cheng,[3] Jeremy Kline,[1] Isaiah Gray,[1] Hil Fung Harry Cheung,[2] Fengyuan Yang,[3] Katja C. Nowack,[4,5,*] and Gregory D. Fuchs[1,5,†]

[1]*School of Applied and Engineering Physics, Cornell University, Ithaca, New York 14853, USA*
[2]*Department of Physics, Cornell University, Ithaca, New York 14853, USA*
[3]*Department of Physics, The Ohio State University, Columbus, Ohio 43210, USA*
[4]*Laboratory of Atomic and Solid State Physics, Cornell University, Ithaca, New York 14853, USA*
[5]*Kavli Institute at Cornell for Nanoscale Science, Ithaca, New York 14853, USA*

(Received 11 October 2022; revised 19 April 2023; accepted 23 May 2023; published 5 June 2023)

Electrical switching of Néel order in an antiferromagnetic insulator is desirable as a basis for memory applications. Unlike electrically driven switching of ferromagnetic order via spin-orbit torques, electrical switching of antiferromagnetic order remains poorly understood. Here we investigate the low-field magnetic properties of 30-nm-thick, *c*-axis-oriented α-Fe_2O_3 Hall devices using a diamond nitrogen-vacancy center scanning microscope. Using the canted moment of α-Fe_2O_3 as a magnetic handle on its Néel vector, we apply a saturating in-plane magnetic field to create a known initial state before letting the state relax in low field for magnetic imaging. We repeat this procedure for different in-plane orientations of the initialization field. We find that the magnetic field images are characterized by stronger magnetic textures for fields along $[\bar{1}\bar{1}20]$ and $[11\bar{2}0]$, suggesting that despite the expected 3-fold magnetocrystalline anisotropy, our α-Fe_2O_3 thin films have an overall in-plane uniaxial anisotropy. We also study current-induced switching of the magnetic order in α-Fe_2O_3. We find that the fraction of the device that switches depends on the current pulse duration, amplitude, and direction relative to the initialization field.

DOI: 10.1103/PhysRevMaterials.7.064402

I. INTRODUCTION

Antiferromagnetic (AFM) materials are interesting for future memory and logic applications due to their subpicosecond spin dynamics [1–3] and their potential for high-density information storage [4]. Because AFM materials have a very small or zero net magnetic moment, direct magnetic manipulation of Néel order is not practical for applications. An attractive approach is to switch Néel order electrically. For example, Néel spin-orbit torque (SOT) induced switching has been reported in the AFM metals CuMnAs [5,6] and Mn_2Au [7–10]. Additionally, Néel order switching observed in CoO [11], NiO [12–15], and α-Fe_2O_3 [16–19] detected by monitoring changes in Hall resistivity has been attributed to SOTs generated at the interface between a heavy-metal layer and an AFM insulator.

One challenge in this research is that purely electrical measurements are difficult to interpret, making it hard to establish the physics behind the current-induced switching. For example, electromigration can influence an electrical signal in a way that mimics a switching-like response [20,21]. Magnetic imaging techniques have been demonstrated as a great tool for understanding the local magnetic order switching in AFM insulators. The application of imaging techniques such as birefringence imaging of NiO [12], x-ray magnetic linear dichroism, photoemission electron microscopy of NiO [13,14] and α-Fe_2O_3 [19], and spin Seebeck microscopy of NiO [22] have improved insights into the properties and behavior of AFM materials.

Among these studies, magnetic imaging of Néel order switching in both NiO and α-Fe_2O_3 have revealed current-induced switching in regions that are outside the current path [12,19], suggesting that SOT is either not or not solely responsible for switching. At the current densities necessary to produce strong SOTs, the substantial Joule heating can induce thermal expansion and thus strain in the AFM layer. Strain can also switch the Néel order without SOT via magnetoelastic coupling [12].

To investigate the magnetism and associated phenomenology of current-induced Néel order switching in an AFM insulator, especially considering the influence of the potentially complicated, nanoscale domain order present in these materials, we use a diamond nitrogen-vacancy (NV) center scanning microscope to image the magnetic order in the canted AFM insulator α-Fe_2O_3. We perform two experiments to study the influence of magnetic field and electric current on the magnetic order of α-Fe_2O_3. First, we study how the orientation of an initializing in-plane magnetic field influences the resulting magnetic state in a low field. We find that the final magnetic state of the sample is influenced by the initialization field direction. In particular, our results are consistent with an in-plane uniaxial anisotropy with Néel vector easy axis

*kcn34@cornell.edu
†gdf9@cornell.edu

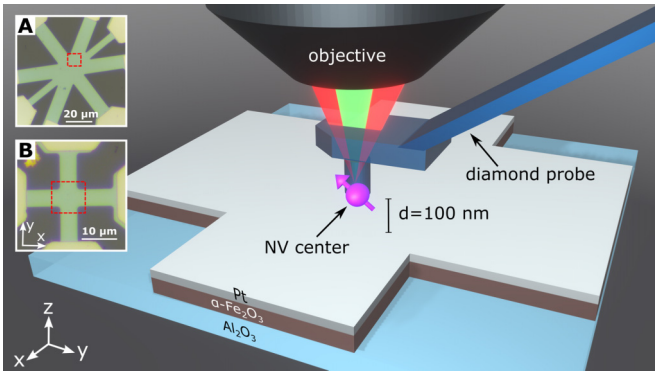

FIG. 1. Schematic of the scanning NV center setup. We use a commercial diamond probe (QZabre LLC) with a single NV center implanted approximately 10 nm below the tip surface. Scans are obtained with a probe-to-sample separation of 100 nm. A microscope objective is used to focus the green excitation beam and collect the red photoluminescence from the NV center. Insets show optical images of device A (top) and B (bottom). The Pt-capped α-Fe_2O_3 appears bright, and the bare Al_2O_3 substrate is dark. The red boxes indicate the 10 μm × 10 μm scan area.

$[\bar{1}100]$ rather than the expected threefold magnetocrystalline anisotropy. Second, we apply current pulses through the Pt layer to investigate current-induced switching. We find that the magnetic order of α-Fe_2O_3 can be switched with current pulses and that the switching efficiency is determined by the current pulse duration, amplitude, and direction relative to the initialization field. Our study presents high-resolution, real-space magnetic field images from α-Fe_2O_3 that shed light on the mechanism of electrically induced magnetic switching in AFM insulators. We discuss this finding in the context of possible switching mechanisms.

II. METHODS

We use a home-built scanning NV center microscope to image the stray magnetic field above α-Fe_2O_3 devices (Fig. 1). Diamond NV centers are sensitive nanoscale magnetometers [23–26] that have been used to image magnetic materials including AFMs [27–33], 2D materials [34], and materials that host skyrmions [35,36]. Antiferromagnetic spin wave dynamics have also been studied using NV centers [37]. Our devices are fabricated from a 30-nm-thick epitaxial α-Fe_2O_3 film grown on an $Al_2O_3(001)$ substrate by off-axis sputtering. 6 nm of Pt is deposited on top of the α-Fe_2O_3 layer *in situ* at room temperature. α-Fe_2O_3 has canted spin order that leads to a weak saturation magnetization of approximately 2 emu/ cm^3. This moment provides a fringe field that is easily detectable using an NV center as a magnetometer (details discussed below and in the Supplemental Material, Sec. I [38]). The entire film stack is patterned into Hall devices to enable electrical measurements. Figure 1 shows optical images of two devices that we study; data from an additional device are included in the Supplemental Material [38]. Device A has six 10-μm-wide leads and two 5-μm-wide leads, while device B has four 5-μm-wide leads. The sample's $[\bar{1}100]$ and $[\bar{1}\bar{1}20]$ axes align with the x and y directions, respectively.

We measure the local magnetic field at the NV center, which is integrated into a scanning probe (Fig. 1) using optically detected magnetic resonance (ODMR). The NV center spin resonance frequency is sensitive to the magnetic field component parallel to the NV axis, which for our probes is oriented at a 54° angle with respect to the sample-plane normal and with an in-plane projection along the x axis. All measurements are made using a ∼20 G bias magnetic field oriented along this direction, with the NV center scanning 110 nm above the sample surface. The microwave excitation field is applied either by driving a microwave current directly through the Pt layer or by a printed circuit board (PCB) resonator below the sample [39]. We use two methods to obtain magnetic images (see Supplemental Material, Sec. II, for details [38]): the dual-iso-B method [28] and the resonance frequency tracking method [40,41]. In dual-iso-B [28], we excite the NV center at two fixed microwave frequencies and measure the difference between their respective photoluminescence (PL) values. From a reference ODMR spectrum, we can calculate the NV center resonance frequency shift, and thus the local magnetic field change. This method, however, is limited to the ∼1.5 G ODMR linewidth. To avoid saturation, we also use resonance frequency tracking [40,41], which adjusts the microwave frequencies at every pixel to track the ODMR peak. All measurements are performed under ambient conditions.

III. RESULTS AND DISCUSSION

A. Magnetic field initialization

First, we study the magnetic field initialization of the sample. Since current-induced magnetic switching measurements are performed at low field, it is important to investigate the sample's low-field magnetic state, how it depends on history, and whether it is influenced by magnetocrystalline anisotropy. We apply a 1 T in-plane magnetic field on the sample, then ramp the field to zero and move the sample into the scanning NV microscope to image the magnetic field above the sample using resonance frequency tracking. We repeat this measurement, rotating the initialization field in-plane by 15° over a total of 360° to study the influence of the initialization field direction on the sample's magnetic state. Figure 2(a) shows examples of the corresponding magnetic images taken on device A. The magnetic images reveal strong features that suggest the presence of a magnetic domain wall (black dashed line), but also more subtle textures reminiscent of magnetic ripples. The images appear qualitatively similar, including the renucleation of a domain wall in nearly the same position, suggesting there is strong pinning that influences the relaxation of the magnetic state from the high-field saturated state to a low-field multidomain state.

The real-space images reveal that, compared to other angles, the magnetic textures are stronger when the initialization field is applied along 0° and 180°, i.e., parallel to the y direction. To quantify this observation, we calculate the standard deviation of the magnetic field pixels (σ_B) inside the red-boxed regions to avoid the magnetic domain wall feature, which otherwise dominates the result. The change of σ_B can be explained by the difference in domain size. Larger domains may appear when the sample is initialized with a magnetic

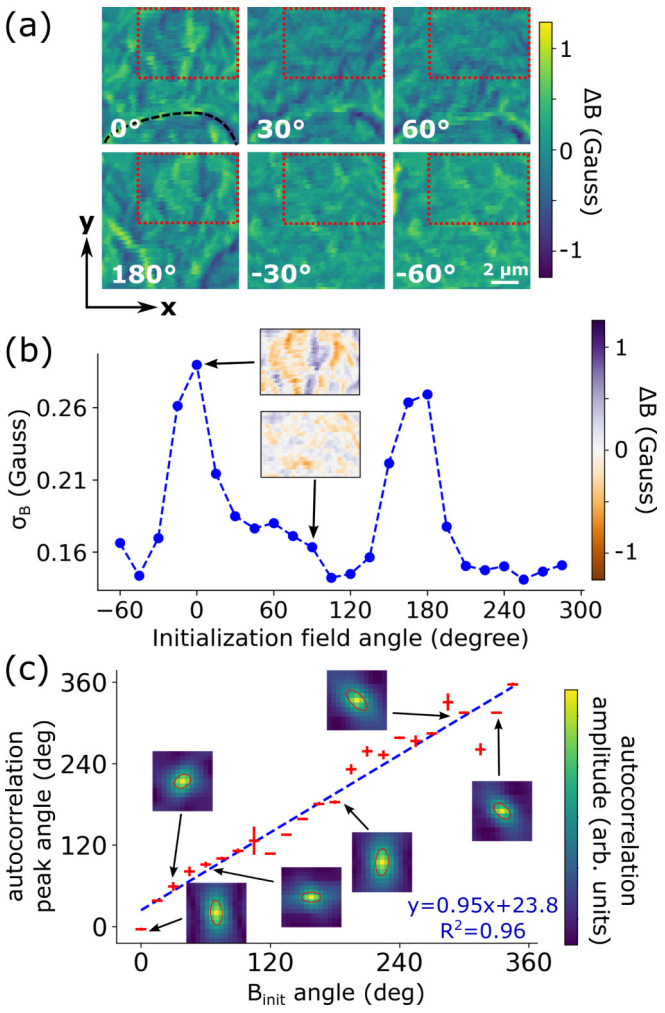

FIG. 2. (a) Examples of magnetic images from device A after it was initialized with a 1 T in-plane magnetic field. The black dashed line indicates a strong domain feature that appears in multiple images. The in-plane angles of the initialization field with respect to the y axis of the image are given in the bottom left corners. Autocorrelation images are calculated from the red-boxed regions. (b) Magnetic field standard deviations of the post-initialization images as a function of the initialization field angle. Peaks are visible for 0° and 180° corresponding to the y and $-y$ direction. Insets are the magnetic images for 0° and 90° initialization field replotted in a diverging color map. The 90° image is more homogeneous than the 0° image. (c) The fitted autocorrelation peak angle as a function of the initialization field angle. The linear fit has a slope of 0.95 and an offset of 23.8°, with an R^2 value of 0.96.

field in an easy axis, and when the initialization field is off an easy axis, the resulting domains may be smaller because there is ambiguity in which direction to relax to at low field. When the small domains are at or near the resolution limit, their magnetic fields partially cancel, leading to images with lower maximum and minimum fields, resulting in smaller σ_B. The plot of σ_B as a function of initialization field angle shows pronounced peaks at 0° and 180° [Fig. 2(b)], suggesting a uniaxial magnetocrystalline anisotropy with the sample's canted moment easy axis in the y direction, and Néel vector easy axis in the x direction. This is in contrast to previous suggestions of threefold anisotropy in α-Fe_2O_3 [16], and is consistent with a previous report of uniaxial anisotropy [17], except with the Néel vector easy axis along $[\bar{1}2\bar{1}0]$, 60° away from our observation. Such sample-to-sample variation may be explained by built-in stresses in thin-film samples.

To understand the initialized magnetic states, it would be ideal to reconstruct the sample magnetization directly from the magnetic images. However, reconstruction of the magnetization from a magnetic field image is an underconstrained problem [29]. Without prior knowledge about the sample's magnetization, for example, whether it is oriented in- or out-of-plane, many solutions may exist that correspond to the same experimental magnetic image. The orientation of the magnetization in α-Fe_2O_3 thin films is still unclear. Previous studies [16,17] assume that the Néel vector for c-axis α-Fe_2O_3 thin films is purely in the sample plane. However, recent x-ray microscopy has revealed that thin films similar to ours also have an out-of-plane magnetic component [19]. Therefore, direct reconstruction will not be single-valued and may not be reliable.

Instead, we further analyze the magnetic textures by calculating the 2-dimensional autocorrelation [42,43]

$$R(\delta x, \delta y) = \sum_{x,y} I(x, y) \cdot I(x + \delta x, y + \delta y),$$

where R is the autocorrelation value, δx and δy are the displacements from the corresponding x and y, and $I(x, y)$ is the pixel intensity at (x, y). The autocorrelation measures the average correlation between one pixel and its surrounding pixels at varied distance. The anisotropy of the center peak of the autocorrelation [see insets in Fig. 2(c)] indicates the preferential orientation of features in the original image. We compute the autocorrelation in the regions marked with red boxes and perform ellipse fitting on contours of the autocorrelation peaks to calculate their rotation angle relative to the vertical direction. Surprisingly, the angle has a linear relationship with the initialization field angle [Fig. 2(c)], suggesting that the sample retains a memory of the direction of the initialization field.

B. Current-induced magnetic order switching

Next, we study how current pulse duration, amplitude, and direction influence current-induced magnetic switching. We first pass a single DC current pulse through the Pt layer of device B using two opposing contacts as the source and drain. We then connect the same contacts to a signal generator to supply the microwave magnetic field needed for magnetic imaging. We acquire a magnetic image using the dual-iso-B method after each current pulse and repeat this process for different current pulse durations and amplitudes. This sequence is performed with three combinations of current and initialization field directions. We subtract the initial magnetic image from the images taken after passing a current pulse to obtain difference images showing local changes of the magnetic field that indicate Néel order switching due to the applied current pulses.

First, we study the effect of current pulse amplitude. We use a pulse duration of 100 μs and vary the amplitude from 3 mA ($j = 1 \times 10^{11}$ A/m^2) to 16 mA ($j = 5.3 \times 10^{11}$ A/m^2) for two initialization field directions and two current directions. Figure 3 shows the resulting magnetic field difference

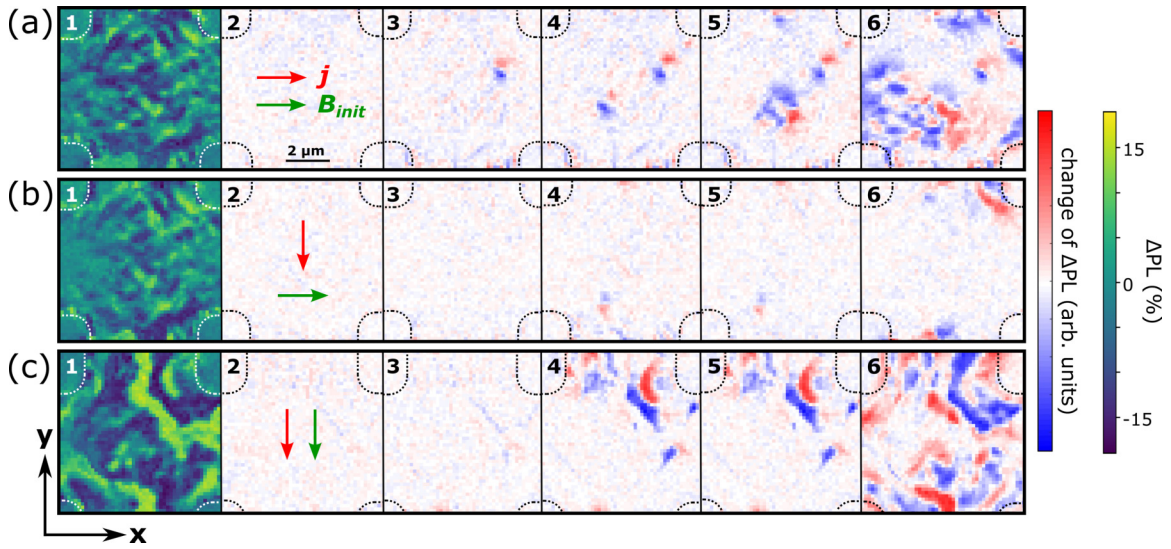

FIG. 3. Magnetic field images acquired using the dual-iso-B method. (1) Image before applying any current pulse. (2)–(6) Difference images obtained by subtracting the scan in (1) from the scan taken after passing 100 μs current pulses with an amplitude of (2) 3 mA, (3) 7 mA, (4) 13 mA, (5) 15 mA, and (6) 16 mA. The green arrows indicate the direction of the initialization field and the red arrows indicate the current pulse direction.

images. For all orientations, a larger fraction of the sample is switched as the current amplitude increases. Comparing the three different combinations of the current pulse and initialization field directions [arrows in Fig. 3(2)], we see that a larger fraction of the sample switches when the current and the initialization field are in the same direction [Figs. 3(a) and 3(c)] than when the two are perpendicular to each other [Fig. 3(b)].

Our field initialization experiment has shown that the initialization field direction influences the resulting low-field magnetic texture. A reasonable speculation is that the canted moment is oriented primarily in the initialization field direction. If so, our observation that a larger fraction of the sample switches when the current and initialization field are parallel indicates that the current pulses tend to rotate the canted moment out of the current direction, i.e., align the Néel order with the current direction. This is consistent with results from previous Hall resistivity measurements [16,17]. Similar switching behavior is also observed by Meer *et al.* [12] in Pt/NiO as a result of a thermal-magnetoelastic effect. This study suggests that the direction of magnetoelastic-effect-induced switching depends on the geometry of the current path, and in a 4-leg device similar to ours, current pulses passing through two opposing contacts rotate the Néel vector to the current direction [12].

To further investigate whether the switching is consistent with magnetic switching induced by thermo-magnetoelastic effects, we analyze the effect of current polarity and pulse duration, with particular attention to the spatial extent of switching in the sample. We observe no significant difference in the magnetic switching induced by current pulses of opposite polarity (see Supplemental Material, Sec. III-C, for details [38]). This observation supports that the switching is primarily induced by heat and strain, rather than SOT. We also study the switching induced by short current pulses and find that switching is induced by a 100 ns, 16 mA pulse, but not a 10 ns, 16 mA pulse (see Supplemental Material, Sec. III-E, for details [38]). The absence of current-induced switching with a 10 ns pulse suggests that switching may require thermal activation. Additionally, we observe switching outside the main current path [Figs. 3(a-6) and 3(c-6), Fig. S9], where SOT is absent. We find that switching occurs in both isolated areas outside the current path and continuously across the current path boundary. Although the latter could be attributed to domain wall pinning-depinning that propagates over many micrometers, all the evidence we gather is consistent with switching induced by a thermal-magnetoelastic effect. These results support that thermal-magnetoelastic effects are sufficient to produce magnetic switching and that SOT may not be the most important mechanism for current-induced switching in our samples.

IV. CONCLUSION

To conclude, we image the stray magnetic field above a thin-film α-Fe_2O_3 device using scanning NV center microscopy. The magnetic images suggest that the orientation of an in-plane 1 T magnetic field influences the sample's magnetic state even after relaxation in a low field. Our results indicate that our α-Fe_2O_3 sample has an in-plane uniaxial anisotropy with a Néel vector easy axis along $[\bar{1}100]$. We electrically switch the Néel order of our sample by applying a current pulse through the thin Pt layer deposited on the α-Fe_2O_3 layer. We find that the most efficient switching happens when the current pulse is in the same direction as the initialization field direction, and current pulses with opposite polarity induce similar switching. Our observations of the current-induced magnetic switching in α-Fe_2O_3 are consistent with the scenario in which the switching is predominantly induced by Joule heating and strain, instead of SOT. Our study offers high-resolution, real-space magnetic images of α-Fe_2O_3 which provides insight into the behaviors of AFM insulator/normal metal bilayers in response to

electric currents. To fully determine the switching mechanism, it will be necessary to separate the effects from SOT and from Joule heating by performing experiments that use ultrashort and high-amplitude current pulses or fabricating devices with SOT-free regions [12]. With a more comprehensive understanding of α-Fe_2O_3's magnetic properties, we can potentially reconstruct the sample's magnetization from magnetic field images, which can provide a complete picture of the magnetic switching process in α-Fe_2O_3.

ACKNOWLEDGMENTS

We thank Dr. Luqiao Liu and Pengxiang Zhang for helpful scientific discussions. This work is primarily supported by the National Science Foundation (Grant No. DMR-2004466). Quantitative peak tracking was developed with support by the U.S. Department of Energy (DOE), Office of Science, National Quantum Information Science Research Centers (Grant No. 1F-60510). The PCB-based microwave resonator was developed with support from the U.S. DOE, Office of Science, Basic Energy Sciences (Grant No. DE-SC0019250). The development of the scanning NV microscope setup was supported by the Cornell Center for Materials Research (CCMR) with funding from the NSF MRSEC program (Grant No. DMR-1719875), including capital equipment support by CCMR and the Kavli Institute at Cornell. Sample growth is supported by the U.S. DOE, Office of Science, Basic Energy Sciences (Grant No. DE-SC0001304).

[1] T. Jungwirth, X. Marti, P. Wadley, and J. Wunderlich, Nat. Nanotechnol. **11**, 231 (2016).
[2] M. B. Jungfleisch, W. Zhang, and A. Hoffmann, Phys. Lett. A **382**, 865 (2018).
[3] V. Baltz, A. Manchon, M. Tsoi, T. Moriyama, T. Ono, and Y. Tserkovnyak, Rev. Mod. Phys. **90**, 015005 (2018).
[4] S. Loth, S. Baumann, C. P. Lutz, D. M. Eigler, and A. J. Heinrich, Science **335**, 196 (2012).
[5] P. Wadley, B. Howells, J. Železný, C. Andrews, V. Hills, R. P. Campion, V. Novák, K. Olejník, F. Maccherozzi, S. S. Dhesi, S. Y. Martin, T. Wagner, J. Wunderlich, F. Freimuth, Y. Mokrousov, J. Kuneš, J. S. Chauhan, M. J. Grzybowski, A. W. Rushforth, K. Edmond *et al.*, Science **351**, 587 (2016).
[6] M. J. Grzybowski, P. Wadley, K. W. Edmonds, R. Beardsley, V. Hills, R. P. Campion, B. L. Gallagher, J. S. Chauhan, V. Novak, T. Jungwirth, F. Maccherozzi, and S. S. Dhesi, Phys. Rev. Lett. **118**, 057701 (2017).
[7] J. Železný, H. Gao, K. Výborný, J. Zemen, J. Mašek, A. Manchon, J. Wunderlich, J. Sinova, and T. Jungwirth, Phys. Rev. Lett. **113**, 157201 (2014).
[8] M. Meinert, D. Graulich, and T. Matalla-Wagner, Phys. Rev. Appl. **9**, 064040 (2018).
[9] S. Y. Bodnar, L. Šmejkal, I. Turek, T. Jungwirth, O. Gomonay, J. Sinova, A. Sapozhnik, H.-J. Elmers, M. Kläui, and M. Jourdan, Nat. Commun. **9**, 348 (2018).
[10] S. Y. Bodnar, M. Filianina, S. P. Bommanaboyena, T. Forrest, F. Maccherozzi, A. A. Sapozhnik, Y. Skourski, M. Kläui, and M. Jourdan, Phys. Rev. B **99**, 140409(R) (2019).
[11] L. Baldrati, C. Schmitt, O. Gomonay, R. Lebrun, R. Ramos, E. Saitoh, J. Sinova, and M. Kläui, Phys. Rev. Lett. **125**, 077201 (2020).
[12] H. Meer, F. Schreiber, C. Schmitt, R. Ramos, E. Saitoh, O. Gomonay, J. Sinova, L. Baldrati, and M. Kläui, Nano Lett. **21**, 114 (2021).
[13] L. Baldrati, O. Gomonay, A. Ross, M. Filianina, R. Lebrun, R. Ramos, C. Leveille, F. Fuhrmann, T. R. Forrest, F. Maccherozzi, S. Valencia, F. Kronast, E. Saitoh, J. Sinova, and M. Kläui, Phys. Rev. Lett. **123**, 177201 (2019).
[14] T. Moriyama, K. Oda, T. Ohkochi, M. Kimata, and T. Ono, Sci. Rep. **8**, 14167 (2018).
[15] X. Z. Chen, R. Zarzuela, J. Zhang, C. Song, X. F. Zhou, G. Y. Shi, F. Li, H. A. Zhou, W. J. Jiang, F. Pan, and Y. Tserkovnyak, Phys. Rev. Lett. **120**, 207204 (2018).
[16] Y. Cheng, S. Yu, M. Zhu, J. Hwang, and F. Yang, Phys. Rev. Lett. **124**, 027202 (2020).
[17] P. Zhang, J. Finley, T. Safi, and L. Liu, Phys. Rev. Lett. **123**, 247206 (2019).
[18] P. Zhang, C.-T. Chou, H. Yun, B. C. McGoldrick, J. T. Hou, K. A. Mkhoyan, and L. Liu, Phys. Rev. Lett. **129**, 017203 (2022).
[19] E. Cogulu, N. N. Statuto, Y. Cheng, F. Yang, R. V. Chopdekar, H. Ohldag, and A. D. Kent, Phys. Rev. B **103**, L100405 (2021).
[20] C. C. Chiang, S. Y. Huang, D. Qu, P. H. Wu, and C. L. Chien, Phys. Rev. Lett. **123**, 227203 (2019).
[21] A. Churikova, D. Bono, B. Neltner, A. Wittmann, L. Scipioni, A. Shepard, T. Newhouse-Illige, J. Greer, and G. S. D. Beach, Appl. Phys. Lett. **116**, 022410 (2020).
[22] I. Gray, T. Moriyama, N. Sivadas, G. M. Stiehl, J. T. Heron, R. Need, B. J. Kirby, D. H. Low, K. C. Nowack, D. G. Schlom, D. C. Ralph, T. Ono, and G. D. Fuchs, Phys. Rev. X **9**, 041016 (2019).
[23] S. Hong, M. S. Grinolds, L. M. Pham, D. Le Sage, L. Luan, R. L. Walsworth, and A. Yacoby, MRS Bull. **38**, 155 (2013).
[24] R. Schirhagl, K. Chang, M. Loretz, and C. L. Degen, Annu. Rev. Phys. Chem. **65**, 83 (2014).
[25] L. Rondin, J. P. Tetienne, T. Hingant, J. F. Roch, P. Maletinsky, and V. Jacques, Rep. Prog. Phys. **77**, 056503 (2014).
[26] D. Hopper, H. Shulevitz, and L. Bassett, Micromachines **9**, 437 (2018).
[27] P. Maletinsky, S. Hong, M. S. Grinolds, B. Hausmann, M. D. Lukin, R. L. Walsworth, M. Loncar, and A. Yacoby, Nat. Nanotechnol. **7**, 320 (2012).
[28] L. Rondin, J.-P. Tetienne, P. Spinicelli, C. Dal Savio, K. Karrai, G. Dantelle, A. Thiaville, S. Rohart, J.-F. Roch, and V. Jacques, Appl. Phys. Lett. **100**, 153118 (2012).
[29] F. Casola, T. van der Sar, and A. Yacoby, Nat. Rev. Mater. **3**, 17088 (2018).
[30] I. Gross, W. Akhtar, V. Garcia, L. J. Martínez, S. Chouaieb, K. Garcia, C. Carrétéro, A. Barthélémy, P. Appel, P. Maletinsky, J.-V. Kim, J. Y. Chauleau, N. Jaouen, M. Viret, M. Bibes, S. Fusil, and V. Jacques, Nature (London) **549**, 252 (2017).

[31] J. Y. Chauleau, T. Chirac, S. Fusil, V. Garcia, W. Akhtar, J. Tranchida, P. Thibaudeau, I. Gross, C. Blouzon, A. Finco, M. Bibes, B. Dkhil, D. D. Khalyavin, P. Manuel, V. Jacques, N. Jaouen, and M. Viret, Nat. Mater. **19**, 386 (2019).

[32] A. Haykal, J. Fischer, W. Akhtar, J. Y. Chauleau, D. Sando, A. Finco, F. Godel, Y. A. Birkhölzer, C. Carrétéro, N. Jaouen, M. Bibes, M. Viret, S. Fusil, V. Jacques, and V. Garcia, Nat. Commun. **11**, 1704 (2020).

[33] M. S. Wörnle, P. Welter, M. Giraldo, T. Lottermoser, M. Fiebig, P. Gambardella, and C. L. Degen, Phys. Rev. B **103**, 094426 (2021).

[34] L. Thiel, Z. Wang, M. A. Tschudin, D. Rohner, I. Gutiérrez-Lezama, N. Ubrig, M. Gibertini, E. Giannini, A. F. Morpurgo, and P. Maletinsky, Science **364**, 973 (2019).

[35] Y. Dovzhenko, F. Casola, S. Schlotter, T. X. Zhou, F. Büttner, R. L. Walsworth, G. S. Beach, and A. Yacoby, Nat. Commun. **9**, 2712 (2018).

[36] I. Gross, W. Akhtar, A. Hrabec, J. Sampaio, L. J. Martínez, S. Chouaieb, B. J. Shields, P. Maletinsky, A. Thiaville, S. Rohart, and V. Jacques, Phys. Rev. Mater. **2**, 024406 (2018).

[37] H. Wang, S. Zhang, N. J. McLaughlin, B. Flebus, M. Huang, Y. Xiao, C. Liu, M. Wu, E. E. Fullerton, Y. Tserkovnyak, and C. R. Du, Sci. Adv. **8**, eabg8562 (2022).

[38] See Supplemental Material at http://link.aps.org/supplemental/10.1103/PhysRevMaterials.7.064402 for experimental details and additional data and analysis.

[39] K. Sasaki, Y. Monnai, S. Saijo, R. Fujita, H. Watanabe, J. Ishi-Hayase, K. M. Itoh, and E. Abe, Rev. Sci. Instrum. **87**, 053904 (2016).

[40] R. S. Schoenfeld and W. Harneit, Phys. Rev. Lett. **106**, 030802 (2011).

[41] P. Welter, B. A. Jósteinsson, S. Josephy, A. Wittmann, A. Morales, G. Puebla-Hellmann, and C. L. Degen, Phys. Rev. Appl. **19**, 034003 (2023).

[42] P. Reith, X. Renshaw Wang, and H. Hilgenkamp, Rev. Sci. Instrum. **88**, 123706 (2017).

[43] G. Nava Antonio, I. Bertelli, B. G. Simon, R. Medapalli, D. Afanasiev, and T. van der Sar, J. Appl. Phys. **129**, 223904 (2021).